**Supplementary Materials**

# Computational engineering of the oxygen electrode-electrolyte interface in solid oxide fuel cells

Kaiming Cheng[1,2], Huixia Xu[2,3,4], Lijun Zhang[4], Jixue Zhou[1,*], Xitao Wang[1], Yong Du[1,4], Ming Chen[2,*]

[1] *Shandong Provincial Key Laboratory of High Strength Lightweight Metallic Materials, Advanced Materials Institute, Qilu University of Technology (Shandong Academy of Sciences), Jinan 250014, China*

[2] *Department of Energy Conversion and Storage, Technical University of Denmark, Lyngby campus, Kgs. Lyngby 2800, Denmark*

[3] *Engineering Research Center of Failure Analysis and Safety Assessment, Shandong Analysis and Test Center, Qilu University of Technology (Shandong Academy of Sciences), Jinan 250014, China*

[4] *State Key Laboratory of Powder Metallurgy, Central South University, Changsha 410083, China*

[*] Corresponding authors: minc@dtu.dk (M. Chen), zhoujx@sdas.org (J.X. Zhou)

## Supplementary Methods

**Construction of the thermodynamic database of the $ZrO_2$-$CeO_2$-SrO system:** The current thermodynamic database of $ZrO_2$-$CeO_2$-SrO is constructed by a careful evaluation of previous CALPHAD modeling [1–3]. A systematic thermodynamic assessment of the $ZrO_2$-$CeO_2$ system was conducted by Du et al. [1] considering all existing experimental data, where the phase relation can be well described by using the ionic sublattice model. Attention should be drawn to the thermodynamic modeling of $ZrO_2$ with a cubic crystal structure, which is unstable without doping e.g. $Y_2O_3$ as yttria stabilized zirconia (YSZ). In order to describe this cubic $ZrO_2$ phase in the current modeling, the thermodynamic parameters for a sublattice model $(Ce^{4+},Zr^{4+})_1(O^{2-})_2$ presented by Du et al. [1] is adopted. This treatment results in a miscibility gap between cubic-$ZrO_2$ and cubic-$CeO_2$, as shown in Supplementary Figure 1a. The here adopted thermodynamic parameters have been utilized to satisfactorily reproduce the experimentally measured interdiffusion profile between CGO and YSZ, as reported in our previous work [4]. The thermodynamic parameters of SrO, with an ionic model in the formula of $(Sr^{2+})_2(Va^{-2},O^{2-})_2$, were taken from Risold et al. [2], who evaluated the experimentally determined information on SrO, such as melting temperature, heat capacity, enthalpy of formation and Gibbs energy of formation. In the current thermodynamic database, the parameters related to $Va^{-2}$ in the second sublattice of $(Sr^{2+})_2(Va^{-2}, O^{2-})_2$ is excluded, since these parameters were originally applied by the authors to keep a consistent treatment with the liquid phase (irrelevant to the current modeling) in the Sr-O system. The perovskite phase $SrZrO_3$ (SZO) was thermodynamically assessed by Gong et al. [3] based on experimental information using the CALPHAD approach. Their parameters can well describe the phase transformation of SZO and reproduce the available thermodynamic properties.

These parameters are recently applied by Gong et al. [5] for the construction of the complete SrO-$ZrO_2$ phase diagram. So, the above parameters are selected to construct the current database, as shown in Supplementary Table 1, with the aim of obtaining a reasonable phase relation while offering precise thermodynamic driving force for simulating the phase transformation. Supplementary Figure 1b gives the isothermal section of the $ZrO_2$-$CeO_2$-SrO system at 1523 K computed using the current thermodynamic database. The experimentally observed formation of interdiffusion zone (IDZ) can be reproduced owing to the solid solubilities located on both of the $ZrO_2$-rich and $CeO_2$-rich ends, and the miscibility gap region assures the existence of interface between $ZrO_2$ (YSZ) and $CeO_2$ (CGO). As more Sr accumulated at this interface at high temperature, the SZO particles start to form as the total amount of Sr increases following a possible dashed arrow line in the Gibbs triangle of the $ZrO_2$-$CeO_2$-SrO system.

**Modeling of the diffusion coefficients:** According to the absolute-reaction rate theory, the atomic mobility of element *k*, $M_k$, may be described by a frequency factor $M_k^0$ and an activation enthalpy $Q_k$ as [6],

$$M_k = exp(\frac{RT\ ln\ M_k^0}{RT})\ exp(\frac{-Q_k}{RT})\frac{1}{RT}\ {}^{mg}\Omega \quad (1)$$

where *R* is the gas constant and *T* is the absolute temperature. ${}^{mg}\Omega$ is a factor taking into account a ferromagnetic contribution to the diffusion coefficient. In the spirit of CALPHAD approach, the composition dependency of item $\Phi_k$ ($\Phi_k$ represents $RT\ ln\ M_k^0 - Q_k$) can be represented with the Redlich-Kister polynomial [7]:

$$\Phi_k = \sum_i x_i \Phi_k^i + \sum_i \sum_{j>i} x_i x_j [\sum_r {}^r\Phi_k^{i,j}(x_i - x_j)]$$
$$+ \sum_i \sum_{j>i} \sum_{k>j} x_i x_j x_k [\sum_s v_{ijk}^s \, {}^s\Phi_k^{i,j,k}] \quad (s = i, j \text{ or } k) \tag{2}$$

where $x_i$ is the mole fraction of species $i$, $\Phi_B^i$ is the value of $\Phi_B$ for pure $i$ and thus represents the value of one endpoint in the composition space. ${}^r\Phi_B^{i,j}$ and ${}^s\Phi_B^{i,j,k}$ are binary and ternary interaction parameters, respectively. Each individual $\Phi$parameter, i.e., $\Phi_B^i$, ${}^r\Phi_B^{i,j}$ or ${}^s\Phi_B^{i,j,k}$, may be expressed as a polynomial in temperature and pressure if necessary. The parameter $v_{i,j,k}^s$ is given by

$$v_{ijk}^s = x_s + \frac{(1 - x_i - x_j - x_k)}{3} \tag{3}$$

where $x_i$, $x_j$, $x_k$ and $x_s$ are mole fractions of elements $i$, $j$, $k$ and $s$, respectively. The interdiffusion coefficients with $n$ as the dependent species are correlated to the atomic mobilities by [6]

$$\widetilde{D}_{kj}^n = \sum_i (\delta_{ik} - x_k) \cdot x_i \cdot M_i \cdot (\frac{\partial \mu_i}{\partial x_j} - \frac{\partial \mu_i}{\partial x_n}) \tag{4}$$

where $\delta_{ik}$ is the Kronecker delta ($\delta_{ik}$=1, if $i = k$, otherwise$\delta_{ik}$=0) and $\mu_i$ is the chemical potential of element $i$. Assuming the monovacancy atomic exchange mechanism, the tracer diffusivity $D_i^*$ relates to the atomic mobility via the Einstein relation:

$$D_i^* = RTM_i \tag{5}$$

The above deals with bulk diffusion, whereas in polycrystalline materials the grain boundary diffusion plays also an important role. Nowadays, the contribution of grain boundary diffusion has been considered in DICTRA [8–10]. The grain boundary diffusion is correlated to the bulk diffusion by using the same frequency factor, but a modified bulk activation energy, as specified by the equation below [11]:

$$M^{\mathrm{gb}} = M_0^{\mathrm{bulk}} \cdot exp(\, F_{\mathrm{GB}} \cdot Q^{\mathrm{bulk}}/R/T) \quad (6)$$

where $M^{gb}$ is the mobility in the grain boundary, $M_0^{bulk}$ and $Q^{bulk}$ are the frequency factor and activation energy in the bulk, respectively, and $F_{GB}$ is the activation energy multiplier. The total mobility including both bulk and grain boundary diffusion is then formulated as:

$$M^{\mathrm{Total}} = \delta/d \cdot M^{\mathrm{gb}} + (1 - \delta/d) \cdot M^{\mathrm{bulk}} \quad (7)$$

where δ, $d$, and $M^{bulk}$ are the grain boundary thickness, the grain size as a function of time and temperature, and the mobility in the bulk, respectively. $F_{GB}$, δ, and $d$ are the input parameters for the grain boundary model in DICTRA. For the terminology of these functions, the readers are referred to the paper by Andersson and Ågren [6].

**Construction of atomic mobility database for the $ZrO_2$-$CeO_2$-SrO system:** Part of the work on the $ZrO_2$-$CeO_2$ system has been reported in our previous work [4], with a short summary provided here. The atomic mobility functions, i.e. $\Phi_k$, of Ce, Zr and Sr in the current $ZrO_2$-$CeO_2$-SrO system were developed via evaluating experimental data using DICTRA. Kilo et al. [12,13] experimentally determined the $^{96}$Zr tracer diffusion in $(Zr_{1-x}Y_x)O_{2-x/2}$ single crystals with $0.15 \leq x \leq 0.48$. They also presented a critical review on the published tracer diffusion coefficients of Zr in YSZ from literature [12–16], where the linear dependence of the zirconium tracer diffusion on the yttria content has been detected within a fairly wide range of stabilizer concentration. In the present work, we use the results of Kilo et al. [12,13] with a stabilizer concentration of 10.2 mol% $Y_2O_3$ to assess the mobility parameter for Zr, considering the similar materials selection to the practical experiments used for current numerical modelling. Bekale et al. [17] determined impurity diffusion of Ce and Gd in single- and poly-crystalline 8YSZ and 10YSZ by analyzing the penetration profiles of a thin film of deposited Ce using secondary ion mass spectrometry (SIMS). The results exhibit a grain

boundary diffusion coefficient higher (about five orders of magnitude) than the bulk diffusion coefficient. The current mobility function of Ce in $ZrO_2$ was evaluated based on the experimental data obtained for 8YSZ [17]. Beschnitt et al. [18] examined the bulk diffusion of Zr in CGO polycrystals by means of Time-of-Flight SIMS, but failed to detect the grain-boundary diffusion since the $CeO_2$ samples were unintentionally doped with Zr through ball-milling the powder with zirconia balls. As for the diffusion of Sr in CGO, Mandt et al. [19] presented an investigation on the $Sr^{2+}$ diffusion along CGO grain boundaries between 600 and 1000 °C, and compared the results with the reported bulk diffusion data collected from previous literature [20–23]. So far, no investigation has been done on the diffusion of Ce in CGO and Sr in YSZ. Considering that both $CeO_2$ and $ZrO_2$ have the same crystal structure of cubic fluorite and are miscible at high temperature, we hence assume that the mobility functions of Ce in CGO and Sr in YSZ are the same as those of Ce in YSZ and Sr in CGO, respectively. We further neglect the influence of Y and Gd, i.e. treat CGO and YSZ as cubic $CeO_2$ and cubic $ZrO_2$, respectively. Supplementary Figures 2a-2d present the calculated tracer diffusion coefficients (bulk and grain boundary) of Zr, Ce and Sr as a function of inversed temperature, compared with the experimental data from literature [13-23]. The calculated bulk and grain boundary diffusion coefficients reproduce the experimental results reasonably well, and the mobility functions of Ce, Zr and Sr in the cubic phase obtained from the current work are listed in Supplementary Table 1.

## Supplementary Figures

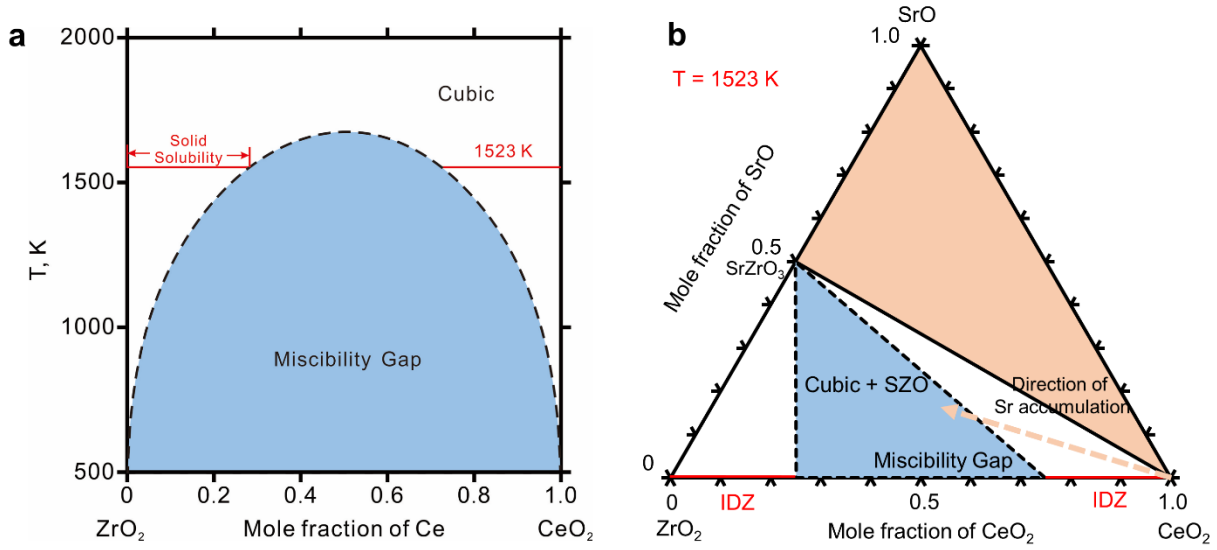


**Supplementary Figure 1:** The (a) $ZrO_2$-$CeO_2$ metastable phase diagram and (b) $ZrO_2$-$CeO_2$-SrO isothermal section (metastable) at 1523 K calculated based on current thermodynamic database.

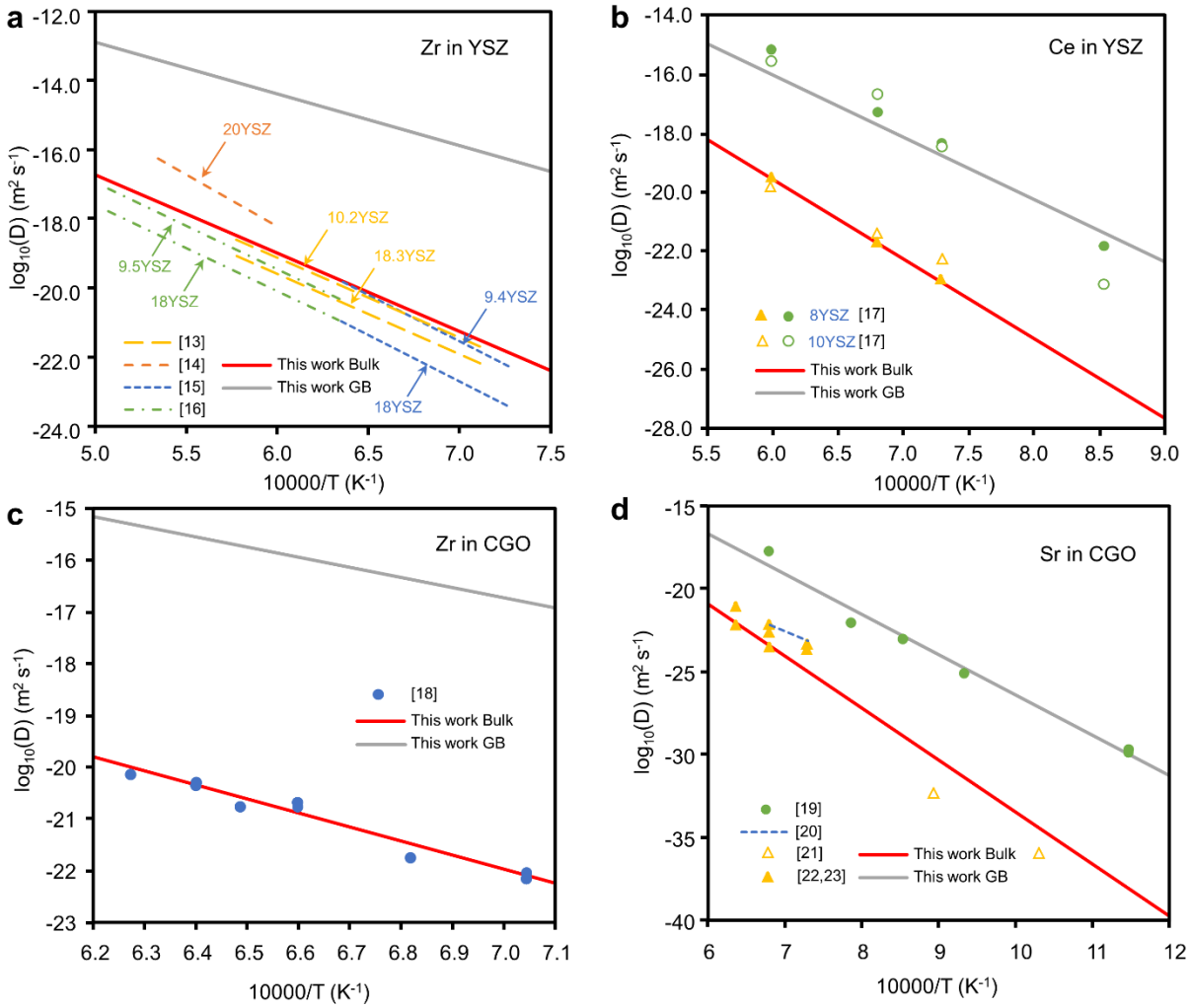


**Supplementary Figure 2:** The calculated tracer diffusion coefficients (bulk and grain boundary) of (a) Zr in YSZ, (b) Ce in YSZ, (c) Zr in CGO and (d) Sr in CGO as a function of inversed temperature, compared with the experimental data from literature [13-23].

## Supplementary Tables

**Supplementary Table 1.** The assessed atomic mobility function $\Phi_k$ in bulk and activation energy multiplier $F_{\mathrm{GB}}$ of the current $ZrO_2$-$CeO_2$-SrO system based on previous experimental data [12-23]. The major elements in the sublattice model are underlined.

| Diffusion component | Function of $\Phi_k$ in bulk | $F_{\mathrm{GB}}$ |
|---|---|---|
| $Zr^{4+}$ in YSZ | $\Phi_{Zr^{4+}}^{(Ce^{4+},\underline{\mathbf{Zr^{4+}}})_1(O^{2-})_2} = -434200 - 103.13T$ | 0.66 |
| $Ce^{4+}$ in YSZ | $\Phi_{Ce^{4+}}^{(Ce^{4+},\underline{\mathbf{Zr^{4+}}})_1(O^{2-})_2} = -516000 - 65.05T$ | 0.78 |
| $Sr^{2+}$ in YSZ | $\Phi_{Sr^{2+}}^{(Ce^{4+},\underline{\mathbf{Zr^{4+}}})_1(O^{2-})_2} = -601476 - 39.30T$ | 0.78 |
| $Zr^{4+}$ in CGO | $\Phi_{Zr^{4+}}^{(\underline{\mathbf{Ce^{4+}}},Zr^{4+})_1(O^{2-})_2} = -518350 - 57.61T$ | 0.72 |
| $Ce^{4+}$ in CGO | $\Phi_{Ce^{4+}}^{(\underline{\mathbf{Ce^{4+}}},Zr^{4+})_1(O^{2-})_2} = -516000 - 65.05T$ | 0.78 |
| $Sr^{2+}$ in CGO | $\Phi_{Sr^{2+}}^{(\underline{\mathbf{Ce^{4+}}},Zr^{4+})_1(O^{2-})_2} = -601476 - 39.30T$ | 0.78 |

## Supplementary References


1. Du, Y., Yashima, M., Koura, T., Kakihana, M. & Yoshimura, M. Thermodynamic evaluation of the $ZrO_2$-$CeO_2$ system. *Scr. Metall. Mater.* **31**, 327–332 (1994).
2. Risold, D., Hallstedt, B. & Gauckler, L. J. The Strontium-oxygen system. *Calphad Comput. Coupling Phase Diagrams Thermochem.* **20**, 353–361 (1996).
3. Gong, W. *et al.* Experimentation and thermodynamic modelling on $SrZrO_3$. *Trans. Nonferrous Met. Soc. China (English Ed.)* **17**, 739–743 (2007).
4. Xu, H. *et al.* Interdiffusion between gadolinia doped ceria and yttria stabilized zirconia in solid oxide fuel cells: Experimental investigation and kinetic modeling. *J. Power Sources* **441**, 227152 (2019).
5. Gong, W., Xie, Y., Zhao, Z., Li, Y. & Navrotsky, A. Thermochemistry of the $ZrO_2$–SrO System: From enthalpies of formation and heat capacities of the compounds to the phase diagram. *J. Am. Ceram. Soc.* **103**, 1425–1435 (2020).
6. Andersson, J. O. & Ågren, J. Models for numerical treatment of multicomponent diffusion in simple phases. *J. Appl. Phys.* **72**, 1350–1355 (1992).
7. Redlich, O. & Kister, A. T. Algebraic Representation of Thermodynamic Properties and the Classification of Solutions. *Ind. Eng. Chem.* **40**, 345–348 (1948).
8. Chen, M. *et al.* Modeling of Ni Diffusion Induced Austenite Formation in Ferritic Stainless Steel Interconnects. *J. Electrochem. Soc.* **164**, F1005–F1010 (2017).
9. Ta, N. *et al.* Numerical simulation of kinetic demixing and decomposition in a $LaCoO_{3-\delta}$ oxygen membrane under an oxygen potential gradient. *J. Memb. Sci.* **548**, 526–539 (2018).

10. Ta, N., Zhang, L., Li, Q., Lu, Z. & Lin, Y. High-temperature oxidation of pure Al: Kinetic modeling supported by experimental characterization. *Corros. Sci.* **139**, 355–369 (2018).
11. Zhang, L. & Chen, Q. CALPHAD-type modeling of diffusion kinetics in multicomponent alloys. in *Handbook of Solid State Diffusion, Volume 1, Diffusion fundamentals and techniques* (eds. Paul, A. & Divinski, S.) 321–362 (Amsterdam Elsevier, 2017).
12. Kilo, M., Borchardt, G., Weber, S., Scherrer, S. & Tinschert, K. Zirconium and calcium tracer diffusion in stabilized cubic zirconia. *Berichte Der Bunsen-gesellschaft - Phys. Chem.* **101**, 1361–1365 (1997).
13. Kilo, M. *et al.* Cation transport in yttria stabilized cubic zirconia: $^{96}Zr$ tracer diffusion in $(Zr_xY_{1-x})O_{2-x/2}$ single crystals with $0.15 \leq x \leq 0.48$. *J. Eur. Ceram. Soc.* **20**, 2069–2077 (2000).
14. Dimos, D. & Kohlstedt, D. L. Diffusional Creep and Kinetic Demixing in Yttria-Stabilized Zirconia. *J. Am. Ceram. Soc.* **70**, 531–536 (1987).
15. Chien, F. & Heuer, A. Lattice diffusion kinetics in $Y_2O_3$-stabilized cubic $ZrO_2$ single crystals: A dislocation loop annealing study. *Philos. Mag. A* **73**, 681–697 (1996).
16. Solmon, H., Chaumont, J., Dolin, C. & Monty, C. Zr, Y and O Self Diffusion In $Zr_{1-x}Y_xO_{2-x/2}$ ($x$ = 0.17). *Ceram. Trans.* **24**, 175–184 (1991).
17. Bekale, V. M., Huntz, A. M., Legros, C., Sattonnay, G. & Jomard, F. Impurity diffusion of cerium and gadolinium in single- and polycrystalline yttria-stabilized zirconia. *Philos. Mag.* **88**, 1–19 (2008).
18. Beschnitt, S. & De Souza, R. A. Impurity diffusion of Hf and Zr in Gd-doped $CeO_2$. *Solid State Ionics* **305**, 23–29 (2017).

19. Mandt, T. *et al.* Sr-diffusion in $Ce_{0.8}Gd_{0.2}O_{2-\delta}$ layers for SOFC application. *Mater. Res. Soc. Symp. Proc.* **1542**, 26–31 (2013).

20. Izuki, M. *et al.* Interfacial stability and cation diffusion across the LSCF/GDC interface. *J. Power Sources* **196**, 7232–7236 (2011).

21. Knibbe, R., Hauch, A., Hjelm, J., Ebbesen, S. D. & Mogensen, M. Durability of Solid Oxide Cells. *Green* **1**, (2011).

22. Sakai, N. *et al.* Interface Stability of Perovskite Cathodes and Rare-Earth Doped Ceria Interlayer in SOFCs. *J. Electrochem. Soc.* **154**, B1331 (2007).

23. Sakai, N. *et al.* Degradation Behavior at Interface of LSCF Cathodes and Rare Earth Doped Ceria. *ECS Trans.* **7**, 389–398 (2019).